PAPER

Complexes *trans*-Pt(BODIPY)X(PEt₃)₂: excitation energy-dependent fluorescence and phosphorescence emissions, oxygen sensing and photocatalysis†

Peter Irmler and Rainer F. Winter*

We report on five new complexes with the general formula *trans*-Pt(BODIPY)X(PEt₃)₂ (**Pt–X**), where the platinum(ɪɪ) ion is σ-bonded to a 4,4-difluoro-4-bora-3a,4a-diaza-*s*-indacen-8-yl (BODIPY) and an anionic ligand X^- (X^- = Cl^-, I^-, NO_2^-, NCS^-, CH_3^-). All five complexes were characterized by multinuclear NMR, electronic absorption and luminescence spectroscopy and by X-ray diffraction analysis. Four of these complexes show efficient intersystem crossing (ISC) from an excited singlet state to a BODIPY-centred T_1 state and exhibit dual fluorescence and phosphorescence emission from the BODIPY ligand. In **Pt–I**, the fluorescence is almost completely quenched, whereas the phosphorescence quantum yield reaches a value of 40%. The rate of ISC and the ratio of phosphorescence to fluorescence emissions depend on the excitation wavelength (*i.e.* on which specific transition is excited). The performance of these complexes as one-component oxygen sensors and their photocatalytic activities were tested by Stern–Volmer quenching experiments and by monitoring the oxidation of 1,5-dihydroxynaphthalene with $^1O_2$ generated from the long-lived triplet state of the sensitizer by triplet–triplet annihilation with $^3O_2$. Exceptionally high $^1O_2$ generation quantum yields of up to near unity were obtained.

Introduction

4,4-Difluoro-4-bora-3a,4a-diaza-*s*-indacene (BODIPY) dyes have been known for three decades for their excellent performances as fluorophores, their versatility and their chemical and photochemical robustness.[1–10] A particularly favourable asset of the BODIPY family of dyes is their modular construction from readily available building blocks, thus allowing for easy implementation of desirable properties or functionalities, *e.g.* for substrate binding, with important implications in the analytical sciences, or fine-tuning of the absorption and emis-

sion wavelengths.[3,11,12] Phosphorescence from BODIPY dyes has, however, only rarely been observed and usually relies on the heavy atom effect of bromine or iodine substituents.[13–16] In particular, there are only a handful of phosphorescent metal–organic BODIPY derivatives, and until very recently, the phosphorescence quantum yields of such compounds did not exceed the rather modest value of 3.5%.[17] In these complexes, the BODIPY dye(s) are either appended to a 2,2′-bipyridine ligand as in **Ru–BDP** or **Ir–BDP** or bonded to Pt(N^C^N) entities with cyclometalating bis(benzimidazol-2-yl)phenyl-derived ligands as in **Pt₂–BDP**, Fig. 1.[3,14,17–19] Much higher quantum yields of up to 31% for the PEt₃ derivative **Pt–Br** (Fig. 1) were achieved in complexes *trans*-Pt(BODIPY)Br(PR₃)₂ (R = Ph, Et) featuring a σ-bonded 4,4-difluoro-4-bora-3a,4a-*s*-indace-nyl dye, which connects to the platinum(ɪɪ) ion *via* its *meso* position.[20] In the latter complexes, the Pt coordination centre acts as a remote heavy metal ion, as the HOMO and the LUMO are heavily biased to the BODIPY ligand and receive only very minor contributions from the coordination centre. As a consequence, the relevant excitation is adequately described as a BODIPY-based π → π* transition with essentially no charge-transfer contributions from the {PtBr(PR₃)₂} fragment. Long-lived excited triplet states of BODIPY dyes are of great interest for applications such as chemical sensing,[16,21,22] triplet–triplet

*Fachbereich Chemie der Universität Konstanz, Universitätsstraße 10,
D-78464 Konstanz, Germany. E-mail: rainer.winter@uni-konstanz.de*

†Electronic supplementary information (ESI) available: Multinuclear NMR spectra of the complexes, packing diagrams with short interatomic contacts, absorption, emission and excitation spectra recorded at different excitation wavelengths, figures displaying oxygen quenching of the phosphorescence emission, changes of the absorption spectra of DHN in the presence of catalytic amounts of MB or **Pt-I** and plots showing the absence of the reaction in the dark; table with the cell parameters and structure refinement data for the complexes; atomic positions for the geometry-optimized structures in the S₀ and the T₁ states and comparison with the experimental structure parameters. CCDC 1474955–1474959. For ESI and crystallographic data in CIF or other electronic format see DOI: 10.1039/c6dt01623e
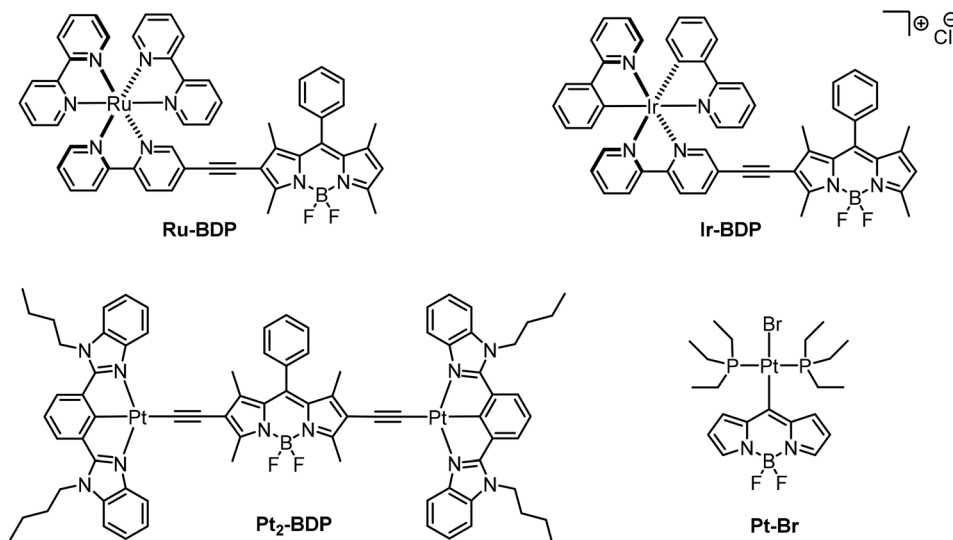
Fig. 1 Molecular structures of room-temperature phosphorescent BODIPY complexes **Ru–BDP**, **Ir–BDP**, **Pt₂–BDP** and **Pt–Br**.

annhilation-based upconversion[17–19,23] and photodynamic therapy.[13,15,24,25] For photodynamic therapy the ability of triplet emitters to transform triplet oxygen ($^3O_2$) to singlet oxygen ($^1O_2$) in a triplet–triplet annihilation process is of pivotal relevance. Its cell toxicity makes the highly reactive $^1O_2$ molecule a powerful weapon against cancer cells.[26–29]

The different structural and electronic influences of a transition metal coligand entity on the photophysical properties of complexes, particularly the phosphorescence quantum yield Φ_{Ph}, are not trivial, though. Decisive factors are the rate constant of the intersystem crossing (k_{ISC}), the ratio of the radiative and non-radiative decay rates, and the thermal accessibility of excited d-states, which typically provide non-radiative deactivation pathways.[30] In the case of square-planar Pt(II) complexes, the relative positioning of the d_{z^2} orbital with respect to the emissive T_1 state is often of crucial relevance.[31] This energy separation largely depends on the ligand-field splitting. Thus, by introducing strong-field ligands, the d_{z^2} orbital can be pushed to higher energy, increasing the energy barrier for non-radiative decay *via* excited d-states.[30–33] In complexes of the type *trans*-Pt(Dye)X(PR₃)₂ (X⁻ = Br⁻, Cl⁻, I⁻ or CN⁻), where Dye represents a σ-bonded thioxanthonyl or a BODIPY attached *via* its *meso* position, the ligand-field splitting can be modulated by the PR₃ ligand and the anionic ligand X⁻.[34] Our previous study has already shown that PEt₃ ligands endow the BODIPY complexes with superior photophysical properties when compared to their PPh₃ counterparts.[20] Here we report our results on five new BODIPY complexes *trans*-Pt(BODIPY)X(PEt₃)₂ with anionic ligands X⁻ that cover a wider range of the spectrochemical series and differ with respect to their *trans*-influence[35] and the results of our investigations into the performance of some representatives as one-component triplet sensors and sensitizers for the photocatalytic oxidation of 1,5-dihydroxynaphthalene (DHN) with molecular oxygen.

Results and discussion

Synthesis and NMR spectroscopy

All complexes were synthesized starting from *cis*-Pt(η²-C₂H₄) (PEt₃)₂, which is obtained by heating *cis*-Pt(Et)₂(PEt₃)₂ in C₆D₆ for 45 min to 114 °C.[36] Oxidative addition of 8-bromo-4,4-difluoro-4-bora-3a,4a-diaza-*s*-indacene (**Br–BODIPY**, see Fig. 2) to the reactive Pt⁰-species is fast at room temperature (r.t.). The resulting complex *cis*-Pt(BODIPY)Br(PEt₃)₂ is then transformed by AgOTf to *trans*-Pt(BODIPY)(OTf)(PEt₃)₂. Subsequent treatment with NaX (X⁻ = Cl⁻, NO₂⁻, NCS⁻) resulted in the replacement of the weakly coordinated OTf⁻ by the respective counter ion and provided complexes **Pt–Cl**, **Pt–NO₂** and **Pt–NCS** (see Fig. 2) in moderate to good yields. Our attempts to introduce a methyl ligand by transmetalation using the Grignard reagent MeMgI failed and the complex *trans*-Pt(BODIPY)I(PEt₃)₂ (**Pt–I**) was formed instead. The use of MgMe₂ as a transmetalating agent was likewise unsuccessful. Reaction of **Pt–OTf** with MeLi finally afforded **Pt–CH₃** (Fig. 2).

^{195}Pt NMR spectra of the *trans*-complexes show a triplet with a coupling constant J_{PtP} in the range of 2692 Hz to 2450 Hz. Correspondingly, the ^{31}P NMR spectra give a singlet for the two *trans*-disposed P donors, which is flanked by the ^{195}Pt satellite doublet with the same J_{PtP} coupling constant. The formation of a direct Pt–C σ-bond is confirmed by the observation of platinum satellites in the ^{13}C NMR spectra, which range from 492 Hz to 409 Hz for J_{PtC} and from 25 Hz to 17 Hz for $^2J_{PtC}$ and $^3J_{PtC}$ couplings, respectively. Some couplings could, however, not be detected due to a low signal-to-noise ratio. The NMR spectra can be found in the ESI, Fig. S1–S23.†

Single crystal X-ray diffraction

Single crystals suitable for X-ray diffraction analysis were obtained for all five Pt complexes. Fig. 3 displays the ORTEP representations of their molecular structures. Relevant bond
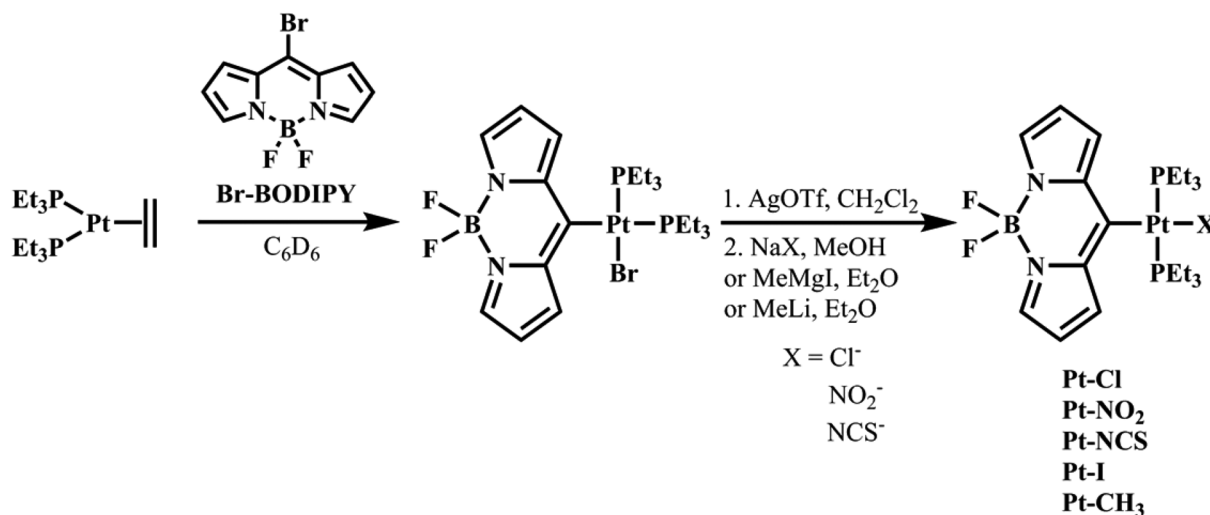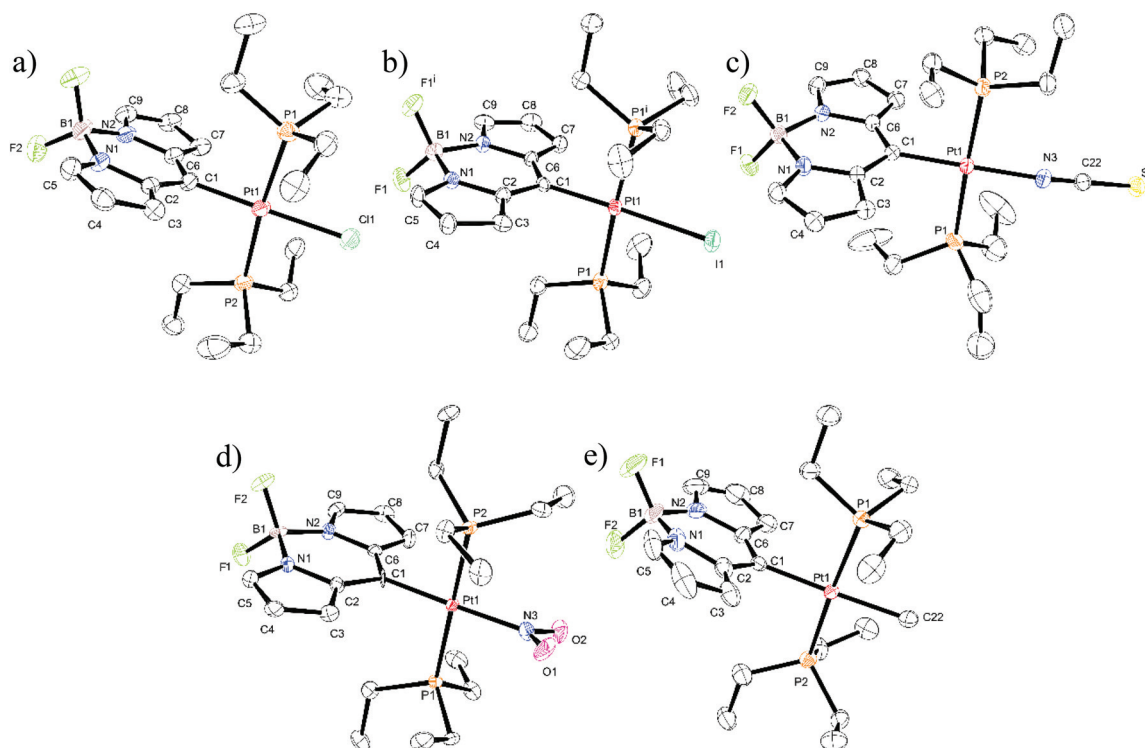
Fig. 2 Synthesis of the complexes **Pt–X**.

Fig. 3 ORTEP representations of the molecular structures of (a) **Pt–Cl**, (b) **Pt–I**, (c) **Pt–NCS**, (d) **Pt–NO₂**, and (e) **Pt–CH₃**. For **Pt–Cl** and **Pt–CH₃** only one of the independent molecules per unit cell are shown. The ellipsoids are drawn at a 40% probability level. Hydrogen atoms are omitted for reasons of clarity. Atom C1 of **Pt–NO₂** remained isotropic and could not be refined further.

lengths and angles can be taken from Table 1, and Table S1 of the ESI† summarizes the crystal and refinement data. **Pt–Cl**, **Pt–NCS**, **Pt–NO₂** and **Pt–CH₃** crystallize in the monoclinic space groups $P2_1/c$, $P2_1/n$, $P2_1/c$, or $P2_1$, respectively. The single crystal of **Pt–I** complies with the symmetry operations of the $Cmc2_1$ space group in the orthorhombic crystal system. The unit cells of **Pt–Cl** and **Pt–CH₃** contain two independent mole-

cules with different sets of bond lengths and angles as given in Table 1.

In the present series of complexes the length of the C1–Pt σ-bond provides a measure for the *trans*-influence and consequently for the σ-donor strength of the anionic ligand X⁻,[35] which increases in the order **Pt–NO₂** < **Pt–Cl** ≈ **Pt–Br** < **Pt–I** ≈ **Pt–NCS** < **Pt–CH₃**. This ordering complies with that of a

Table 1 Selected bond lengths [Å] and bond angles [°] of the complexes *trans*-Pt(BODIPY)X(PEt₃)₂ (**Pt–X**) and of Pt–Br[20]

	Pt–Br		Pt–Cl		Pt–I	Pt–NCS	Pt–NO₂	Pt–CH₃	
	Molecule 1	Molecule 2	Molecule 1	Molecule 2				Molecule 1	Molecule 2
Bond lengths/Å									
C1—Pt1	1.984(10)	1.964(11)	1.976(7)	1.971(8)	1.994(10)	1.984(4)	1.956(9)^c	2.039(11)	2.053(12)
X—Pt1^a	2.4973(12)	2.5118(12)	2.3750(19)	2.385(2)	2.6689(8)	2.048(4)	2.019(8)	2.127(12)	2.137(11)
P1—Pt1	2.315(3)	2.320(3)	2.319(2)	2.316(2)	2.3206(15)	2.3135(13)	2.329(2)	2.299(3)	2.304(3)
P2—Pt1	2.327(3)	2.324(3)	2.309(2)	2.310(2)	2.3206(15)^b	2.3249(11)	2.334(2)	2.290(3)	2.285(3)
Bond angles/°									
C1–Pt1–P1	93.7(3)	92.9(3)	91.2(2)	91.6(2)	91.37(7)	91.44(12)	92.3(3)^c	91.3(3)	90.7(3)
C1–Pt1–P2	91.3(3)	90.5(3)	94.0(2)	93.0(2)	91.37(7)^b	90.79(12)	89.3(3)^c	91.9(3)	92.7(3)
P1–Pt1–X^a	87.73(8)	88.41(8)	87.13(7)	87.68(8)	88.71(7)	87.28(12)	88.6(2)	86.3(3)	86.7(3)
P2–Pt1–X^a	87.28(8)	88.16(8)	87.61(7)	87.76(8)	88.71(7)^b	90.62(11)	90.0(2)	90.5(3)	89.9(3)
P1–Pt1–P2	175.01(11)	176.02(11)	174.74(8)	175.00(7)	176.8(3)	177.17(5)	173.83(8)	176.05(12)	176.57(12)
C1–Pt1–X^a	178.6(3)	178.6(3)	178.3(2)	179.0(2)	176.03(8)	175.77(17)	178.2(4)^c	177.6(4)	177.2(5)

^{a} X represents the donor atom of the anionic ligand in *trans*-position to the dye at the Pt ion. ^{b} The molecule has a mirror plane which is defined by the plane of the dye's inner heterocycle. ^{c} Atom C1 could not be refined anisotropically.

related series of platinum complexes with a σ-bonded perylene or perylene monoimide dye.[37] For **Pt–CH₃** the difference between the Pt–C bond lengths to the methyl (2.127(12) or 2.137(11) Å) and the BODIPY ligands (2.039(11) or 2.053(12) Å for the two independent molecules of the unit cell) reflects the difference of the covalent radii of a sp³ and a sp² carbon atom. Similar differences have *e.g.* been observed for *trans*-Pt(CH₃)(Ph)(PPh₃)₂ d(Pt–CH₃) = 2.226(4) Å, d(Pt–Ph = 2.058(4) Å).[38] The Pt–Me bond of **Pt–CH₃** is expectedly longer than in complexes *trans*-Pt(CH₃)Cl(PR₃)₂ owing to the opposite placement of two σ-carbyl ligands, which both exert a strong σ-*trans*-influence (*cf.* 2.08(1) Å for R = Ph or 2.069(8) Å for R = C₆H₄F-4).[39,40]

With deviations of 2.8° to 6.2° for the angle P1–Pt–P2 and 1.0° to 4.2° for bond angle C1–Pt–X (X = donor atom of the anionic ligand) and a maximum deviation of 4.0° for *cis*-angles X–Pt–P and C1–Pt–P from the ideal values and a coplanarity of all donor atoms with the Pt(ɪɪ) ion the coordination centre exhibits a close to ideal square planar coordination geometry. This is also indicated by the summations of bond angles at the Pt(ɪɪ) ion, which range from 359.94° to 360.20°. The P1–Pt–P2 angle opens to the side of the sterically demanding BODIPY ligand.

The various steric and electronic influences of a PtL₃ fragment for tipping the scale towards either κ*N* or κ*S* coordination of a thiocyanate ligand are textbook examples for the phenomenon of coordination isomerism.[41,42] *N* coordination in spite of the soft character of the {Pt(BODIPY)(PEt₃)₂} fragment is here favoured by the strong *trans*-influence of the opposite carbyl ligand, the light donor atom, and by steric effects. Thus, *N* coordination maintains a near coincidence of the NCS⁻ axis with the C1–Pt–N vector Pt–N3–C22 = 162.2(4)°, S1–C22–N3 = 179.7(4)°, thus avoiding unfavourable steric interactions with the *cis*-disposed PEt₃ ligands (Fig. 3c). *N* coordination of the NCS⁻ ligand has likewise been observed in the related perylene complex of Espinet and coworkers.[37]

Packing diagrams of individual molecules in the crystal lattice are shown in Fig. S24–S28 of the ESI.† All structures exhibit several short intermolecular contacts. Most prevalent are hydrogen bonding interactions H···F–B between pyrrolic or methyl protons and the BF₂⁻ fluorine atoms. These latter contacts are in the range of 2.330 to 2.539 Å, which is by 0.330 to 0.131 Å shorter than the sum of the van der Waals radii. Most notably, H···F contacts to methyl hydrogens of the PEt₃ ligands are frequently shorter than those to the hydrogen atoms attached to the heterocycles. These hydrogen bonds are sometimes augmented by C–H···π interactions between methyl protons and a pyrrolic carbon atom ranging from 2.634 to 2.757 Å. In several cases, additional contacts exist between pyrrolic or methyl protons and heteroatoms of the anionic ligand X⁻, most importantly to the oxygen atoms of the nitrite ligand of **Pt–NO₂** (2.378 to 2.487 Å with the shorter contacts again to PEt₃ methyl protons), the S atom of the κ*N*-thiocyanate ligand in **Pt–NCS** (2.842 and 2.921 Å) or, very weakly, to the I⁻ ligand in **Pt–I** (3.127 Å). The latter complex exhibits an interesting brick-wall packing in the *ac* plane, where individual molecules associate weakly along the *c* axis *via* C–H···I interactions and, more strongly so, along the *a* axis by CH···π interactions between the pyrrolic carbon atom C9 and a PEt₃ methyl proton of neighbouring molecules positioned above and below (C–H···C = 2.684 Å, see Fig. S25b of the ESI†). The structural relevance of CH···π interactions has recently been highlighted.[43]

UV-vis spectroscopy, TD-DFT calculations and luminescence properties

The UV-Vis absorption spectra of complexes **Pt–Cl** to **Pt–CH₃** are shown in Fig. 4. They are dominated by the sharp, vibrationally structured band of the attached BODIPY dye with extinction coefficients ε of 52 600 to 57 400 M⁻¹ cm⁻¹. Peaking at a narrow range of 461 to 472 nm (Table 2), the position is almost invariant to the identity of the ligand X⁻. At higher energies in the near UV another weaker, asymmetric absorption is observed at λ = 370 to 300 nm with a maximum extinction coefficient of *ca.* 11 000 M⁻¹ cm⁻¹. In some cases that feature is resolved into two distinct bands which are separated
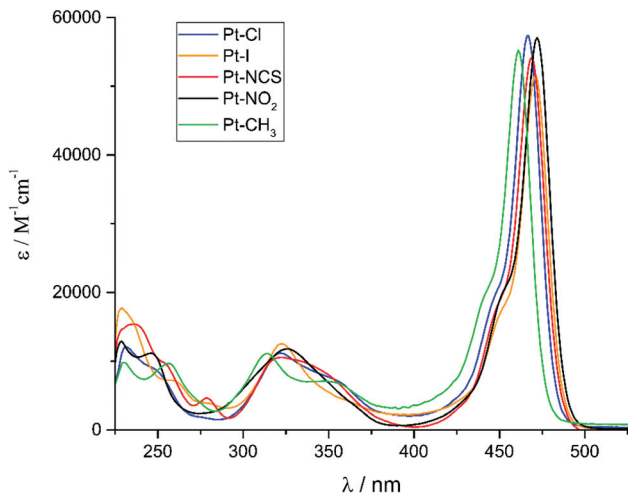
Fig. 4 Electronic absorption spectra of **Pt–Cl**, **Pt–I**, **Pt–NCS**, **Pt–NO₂** and **Pt–CH₃** in a *ca*. 10^{-5} M CH_2Cl_2 solution at 298 K.

by 20 to 30 nm. Time-dependent DFT (TD-DFT) calculations carried out on geometry optimized structures accordingly predict two separate absorptions in this energy range. The comparison of experimental and calculated TD-DFT data in Table 2 shows that our calculations reproduce the general absorption features well but overestimate the energy of the prominent BODIPY-based $\pi \to \pi^*$ transition by *ca*. 4200 cm^{-1}. The TD-DFT data reveal that the intense band at the lowest energy arises from the HOMO $\to$ LUMO transition. As it is evident from the graphical depictions of the relevant orbitals of **Pt–NO₂** and **Pt–I** in Fig. 5 and the compilation in Tables 2 and 3, the latter is adequately described as a $\pi \to \pi^*$ transition of the BODIPY ligand with only very small contributions of the {PtX(PEt₃)₂} fragment. This also explains the negligible influence of the X⁻ ligand on the transition energies. The absorption near 320 nm originates from two energetically close-lying transitions (HOMO−5 →

LUMO, HOMO−6 → LUMO for **Pt–I**, HOMO−6 → LUMO, HOMO−7 → LUMO/HOMO−8 → LUMO for **Pt–NO₂**, Table 2). One has distinct Pt(PEt₃)₂ → BODIPY charge-transfer (CT) character, while the second one involves another $\pi \to \pi^*$ transition within the dye ligand. As we will see later, the more significant metal contribution to the higher energy transition has important implications on the intersystem crossing rate constants k_{ISC} from the different excited states.

Table S15 of the ESI† compares the calculated structure parameters of complexes **Pt–Cl**, **Pt–I**, **Pt–NCS**, and **Pt–NO₂** to the experimental data from X-ray crystal diffraction and to those calculated for the T_1 state. Calculated bond parameters for the S_0 state retrace experimentally observed bond lengths and angles well. The only structural difference between the T_1 and the S_0 states is a slight elongation of the Pt–C1 bond by 2–3 pm while all other bond lengths and bond angles remain essentially unaffected.

Like the previously reported complex **Pt–Br**[20] all complexes exhibit dual fluorescence at $\lambda \approx 480$ nm and phosphorescence at $\lambda \approx 640$ nm when excited into their lowest energy absorption band. Emission spectra of the complexes and of **Br–BODIPY** are compared in Fig. 6 while relevant photophysical data are collected in Table 4. The small Stokes shifts of <500 cm^{-1} and luminescence decay rates in the subnanosecond range are typical assets of BODIPY-based fluorescence emissions. The congruence of electronic absorption and excitation spectra as documented in Fig. S29–S33 of the ESI† and the blue shift of the fluorescence peaks compared to that of the **Br–BODIPY** precursor ($\lambda_{Fl} = 517$ nm) demonstrate, that both emissions originate from the complexes and not from impurities or unreacted **Br–BODIPY**. That blue shift has been traced to a preferential lifting of the BODIPY LUMO owing to a slightly larger contribution of the strongly electron-donating {Pt(PEt₃)₂X} moiety[44] to the receptor orbital.[20] The long lifetimes of 162 to 439 μs at r.t. and the large Stokes shifts of *ca*. 5600 cm^{-1} characterize the low-energy emission band as phosphorescence

Table 2 Absorption data of complexes **Pt–Cl**, **Pt–I**, **Pt–NCS**, **Pt–NO₂** and **Pt–CH₃** in *ca*. 10^{-5} M CH_2Cl_2 solutions at 298 K and TD-DFT calculations in CH_2Cl_2

	Absorption data	TD-DFT data			
	λ_{max} [nm] ($\varepsilon \times 10^{-3}$ [$M^{-1}\ cm^{-1}$])	λ [nm]	Major contributions [%]	f^a	Assignment
Pt–Cl	321 (11.1), 340 (7.4), 467 (57.4)	293	H−6 → LUMO (93)	0.16	$\pi \to \pi^*$ (BODIPY)
		310	H−5 → LUMO (81)	0.10	Pt(PEt₃)₂ → BODIPY CT
		390	HOMO → LUMO (97)	0.39	$\pi \to \pi^*$ (BODIPY)
Pt–I	322 (12.5), 352 (4.3) 471 (52.6)	295	H−6 → LUMO (90)	0.17	$\pi \to \pi^*$ (BODIPY)
		309	H−5 → LUMO (81)	0.07	Pt(PEt₃)₂ → BODIPY CT
		392	HOMO → LUMO (97)	0.39	$\pi \to \pi^*$ (BODIPY)
Pt–NCS	320 (10.5), 337 (9.2), 469 (54.2)	294	H−6 → LUMO (93)	0.18	$\pi \to \pi^*$ (BODIPY)
		310	H−5 → LUMO (88)	0.07	Pt(PEt₃)₂ → BODIPY CT
		393	HOMO → LUMO (95)	0.37	$\pi \to \pi^*$ (BODIPY)
Pt–NO₂	325 (11.7), 472 (57.0)	265	H−8 → LUMO (39)	0.08	Pt(NO₂)(PEt₃)₂ → BODIPY CT
			H−7 → LUMO (56)		Pt(NO₂)(PEt₃)₂ → BODIPY CT
		294	H−6 → LUMO (90)	0.17	$\pi \to \pi^*$ (BODIPY)
		392	HOMO → LUMO (97)	0.40	$\pi \to \pi^*$ (BODIPY)
Pt–CH₃ ^{b}	314 (11.1), 346 (7.1) 461 (55.2)	n.c.			

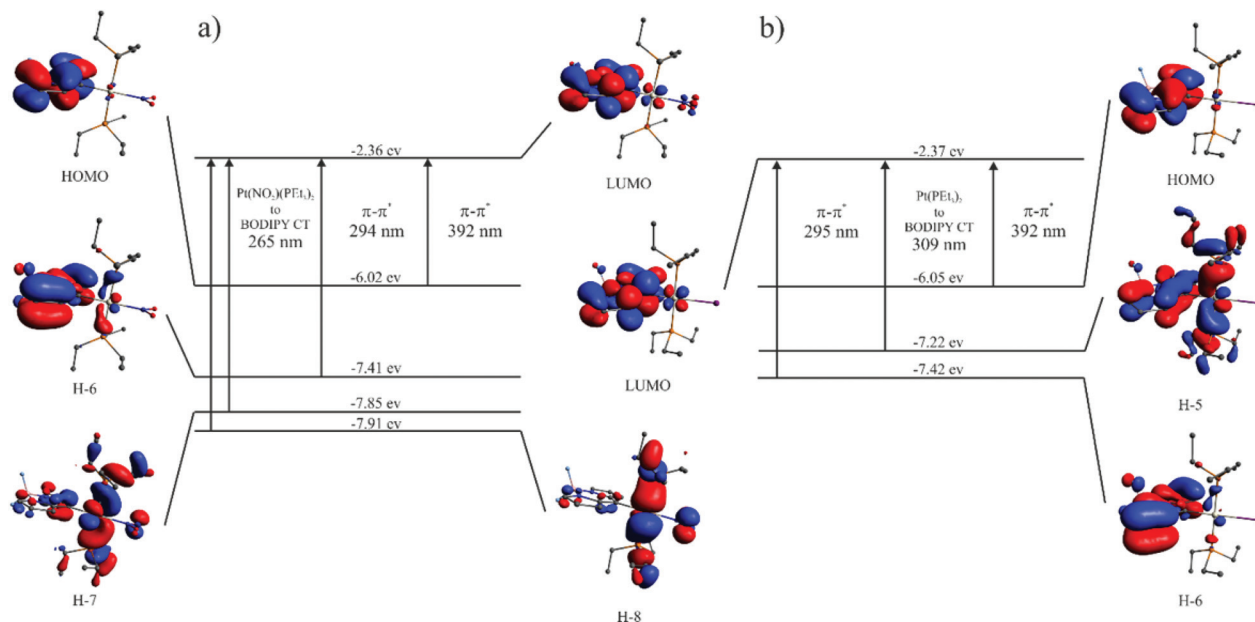^{a} Oscillator strength. ^{b} n.c. = not calculated.

Fig. 5 Energies and graphical representations of the relevant molecular orbitals along with calculated electronic transitions of (a) **Pt–NO₂** and (b) **Pt–I**.

Table 3 Calculated Mulliken parameters of **Pt–Cl**, **Pt–I**, **Pt–NCS** and **Pt–NO₂** [a]

		Pt	BODIPY	PEt$_3$	X^{-} [b]
Pt–Cl	LUMO	4	94	2	0
	HOMO	1	98	1	0
	H−5	16	43	40	1
	H−6	2	95	3	0
	Spin density[c]	0.012	1.975	0.017	−0.004
Pt–I	LUMO	3	94	2	0
	HOMO	1	98	1	0
	H−5	14	47	39	0
	H−6	3	92	5	1
	Spin density[c]	0.009	1.978	0.019	−0.006
Pt–NCS	LUMO	3	94	2	1
	HOMO	1	98	1	0
	H−5	18	41	41	0
	H−6	2	93	5	0
	Spin density[c]	0.003	1.978	0.020	0.000
Pt–NO₂	LUMO	3	93	2	2
	HOMO	1	98	1	0
	H−6	3	90	7	0
	H−7	40	16	37	7
	H−8	50	6	31	13
	Spin density[c]	−0.003	1.982	0.020	0.001

[a] Percent contributions of the given fragments. [b] X^{-} represents the anionic ligand in *trans*-position to the dye at the Pt ion. [c] Spin density contribution of the respective fragment to the spin density surface.

Fig. 6 Emission spectra of **Pt–Cl**, **Pt–I**, **Pt–NO₂** **Pt–NCS** and **Br–BODIPY** in degassed CH$_2$Cl$_2$ solutions at concentrations of *ca.* 10^{-6} M upon irradiation into the lowest energy absorption band of the complexes.

(Table 4). From the comparison of emission spectra in Fig. 6 and the data in Table 4 it becomes immediately apparent that larger phosphorescence quantum yields Φ_{Ph} go along with a decrease of those of the fluorescence emission Φ_{Fl} and *vice versa*. No luminescence data could be obtained for **Pt–CH₃**, as this complex decomposed when irradiated in the fluorescence spectrometer. Fig. S34 of the ESI† illustrates that the decompo-
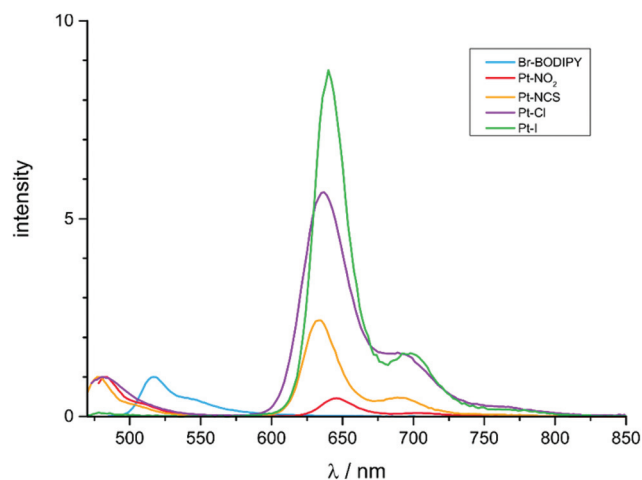
sition product still constitutes a BODIPY dye. The distinct redshift of the fluorescence peak and its similar position to that of the **Br–BODIPY** precursor suggest that the BODIPY-ligand is detached from the Pt atom during photochemical degradation. Facile Pt-BODIPY bond breaking in this complex is likely caused by the strong σ-*trans*-influence of the methyl ligand and the concomitant weakening of the Pt-C(BODIPY) σ-bond, which is even amplified in the excited T$_1$ state (Tables 1 and S15 of the ESI†).

The ratio of phosphorescence to fluorescence intensities increases in the order **Pt–NO₂** < **Pt–NCS** < **Pt–Cl** < **Pt–I**; **Pt–Br**

Table 4 Luminescence data of **Pt–Br**,[20] **Pt–Cl**, **Pt–I**, **Pt–NO₂** and **Pt–NCS** in N₂ saturated CH₂Cl₂ and toluene solutions, respectively, at concentrations of *ca.* 10^{-6} M. If not stated otherwise the samples were excited into the lowest energy absorption band

	$\lambda_{max,Fl}$ [nm] (Stokes shift [cm^{-1}])	$\lambda_{max,Ph}$ [nm] (Stokes shift [cm^{-1}])	$\Phi_{Fl,exc467}$ $(\Phi_{Fl,exc322})^a$	$\Phi_{Ph,exc467}$ $(\Phi_{Ph,exc322})^a$	τ_{Fl} [ns]	τ_{Ph} [μs]
Pt–Br[20]	479 (491)	637 (5669)	0.011	0.312	n.d.^{b}	162
Pt–Cl	478 (493)	633 (5615)	0.016 (0.005)	0.349 (0.356)	0.174	277
	479 (491)^c	631 (5520)^c				243^c
	478^d	626^d				450^d
Pt–I	481 (441)	641 (5631)	0.002 (0.000)	0.364 (0.397)	0.484	297
Pt–NO₂	483 (483)	645 (5683)	0.115 (0.052)	0.166 (0.209)	0.470	439
Pt–NCS	480 (489)	637 (5623)	0.048 (0.024)	0.244 (0.323)	1.027	313

^{a} Fluorescence and phosphorescence quantum yields measured at an excitation wavelength of 467 nm or 322 nm, respectively. ^{b} Not determined. ^{c} Measured in toluene solution at r.t. ^{d} Measured in a toluene glass at 77 K.

occupies a position intermediate between **Pt–NCS** and **Pt–Cl**. This ordering parallels an increasing *trans*-influence of the ligand X$^-$,[35] but shows no clear correlation to its positioning within the spectroelectrochemical series. This indicates that thermal population of excited d-states is most probably not the dominant pathway for radiationless decay of the excited states, although the documented complexities of such processes still warrant caution.[30]

As the already very weak fluorescence of **Pt–I** was found to vanish altogether on excitation into the high-energy absorption band at 322 nm, the intensities of the phosphorescence and fluorescence emissions were monitored at different excitation wavelengths. Fig. 7a and b illustrate that, on irradiation into the higher energy absorption band(s), the phosphorescence quantum yield Φ_{Ph} of **Pt–NO₂** further increases at the expense of that of the fluorescence emission (Φ_{Fl}). The notion that the ratio of phosphorescence and fluorescence emission intensities may depend on the excitation wavelength has been perspectively proposed by Chou *et al.*[33] and was experimentally demonstrated soon after.[45–47] This phenomenon relies on the different involvement of a heavy atom in the different excited states. In particular, a larger degree of charge-transfer between a metal/coligand entity and the emissive ligand (metal-to-ligand or ligand-to-metal charge-transfer) provides a more direct pathway for ISC, and hence a larger rate constant k_{ISC}, than the remote heavy-metal effect alone.[45,46,48] The efficiencies of the ISC from a higher-lying S_n state ($S_n \rightarrow T_m \rightarrow T_1$) and from the S_1 state ($S_n \rightarrow S_1 \rightarrow T_1$) may thus drastically differ if the initially populated states differ in character.

For the BODIPY-centred excited S_1 state, which is initially populated by irradiation into the prominent HOMO → LUMO $\pi \rightarrow \pi^*$ absorption band, the coordination centre merely acts as a remote heavy metal atom, and the efficiency of ISC relies on the close proximity of the Pt ion to the dye (note that k_{ISC} in that case relates to r^{-6} where r is the distance of the heavy metal atom to the midpoint of the dye).[47] This is readily inferred from the spin density surfaces for the excited triplet states of **Pt–Cl**, **Pt–I**, **Pt–NCS**, and **Pt–NO₂** in Fig. 8. Complying with the compositions of the HOMO and the LUMO, almost the entire spin density resides at the BODIPY ligand with only very modest contributions of 0.3% to 1.2% from the Pt ion. As it was already discussed, the higher energy absorption band,
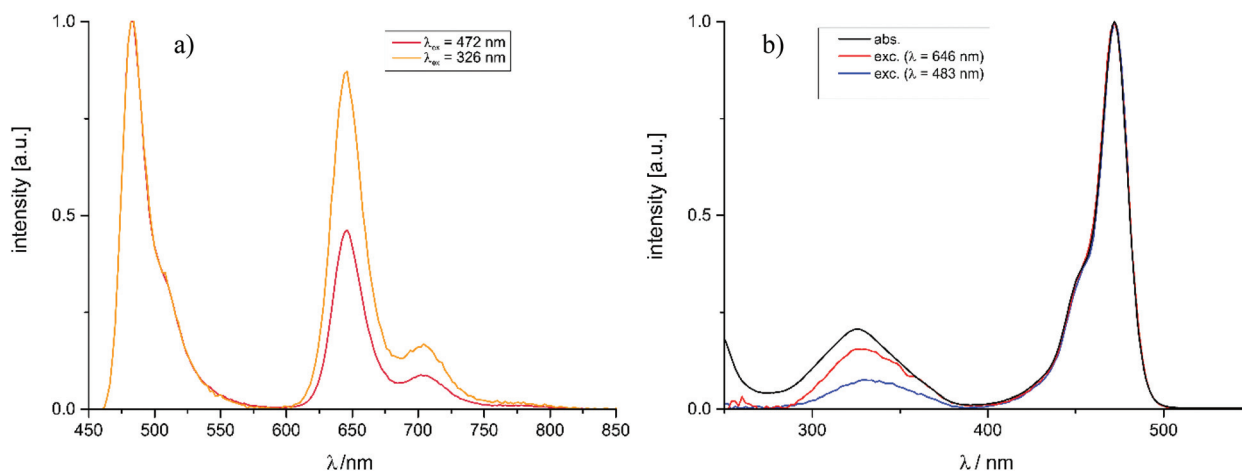
Fig. 7 (a) Emission spectra of **Pt–NO₂** on excitation at $\lambda = 326$ nm and $\lambda = 472$ nm, respectively. (b) Absorption and excitation spectra of **Pt–NO₂**. The excitation spectra were recorded for the fluorescence band at 483 nm and the phosphorescence band at 646 nm. Measurements were performed on degassed CH₂Cl₂ solutions at concentrations of *ca.* 10^{-6} M.
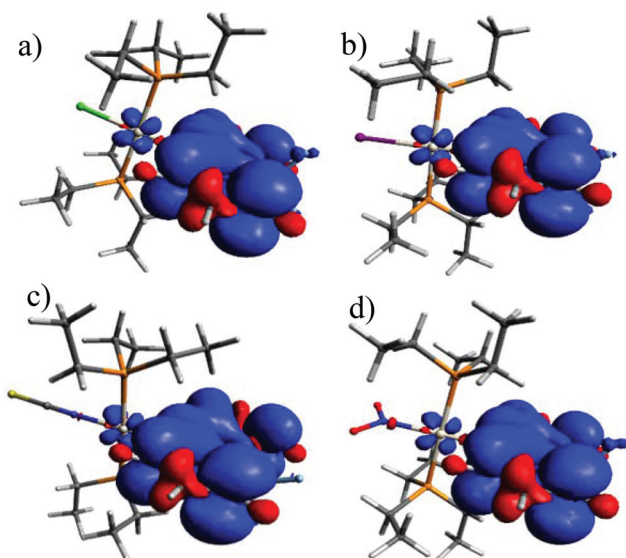
Fig. 8 Spin density surfaces of the T_1 state of (a) **Pt–Cl**, (b) **Pt–I**, (c) **Pt–NCS**, and (d) **Pt–NO$_2$**.

Fig. 9 Stacked luminescence spectra of **Pt–I** in CH_2Cl_2 solution at different oxygen concentration levels.

populating (a) higher S_n state(s), has more significant contributions from Pt(PEt$_3$)$_2$ → BODIPY charge-transfer (ML → L'CT, Fig. 5 and Tables 2 and 3). As is illustrated in Scheme 1, the faster $k_{ISC,n}$ from the higher-lying ML → L'CT excited state provides an even more competitive pathway for population of the phosphorescent T_1 state than ISC from S_1. Excitation into (a) higher S_n state(s) thus decreases the fluorescence quantum yield Φ_{Fl} while further boosting Φ_{Ph}. The highest phosphorescence quantum yields are found for the simple halogenido complexes. The values of Φ_{Ph} of 36.4% or 39.7% for **Pt–I** on excitation at 467 or at 322 nm, respectively, are, to the best of our knowledge, the highest phosphorescence quantum yields of any BODIPY derivative, even surpassing those of **Pt–Br**.[20]

Emission quenching by $^3O_2$ and $^1O_2$ generation

The very long lifetimes of the excited triplet states of up to 439 μs make these compounds interesting candidates for applications such as triplet molecule sensing and photocatalysis. Their capabilities to act as one-component sensors for
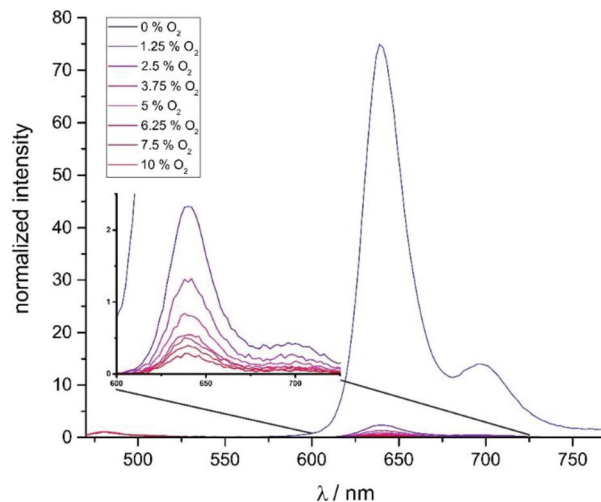
triplet molecules were tested by Stern–Volmer quenching experiments using $^3O_2$ as the quencher. Fig. 9 and as Fig. S35 and S37 of the ESI† illustrate the results of such experiments for **Pt–I**, **Pt–Cl** and **Pt–NO$_2$**. The Stern–Volmer equation is given as $I_0/I = 1 + K_{SV}[O_2]$, where I_0 is the luminescence intensity under exclusion of oxygen, I is the luminescence intensity at a specific oxygen concentration, and K_{SV} is the Stern–Volmer quenching constant, which is a measure for the sensitivity of the sensor. Fig. 10 displays plots of $(I_0/I) − 1$ and $(\tau_0/\tau) − 1$ as a function of the partial oxygen pressure ($p(O_2)$). The quenching constants of $K_{SV} = 2380 \pm 170$ bar^{-1} for **Pt–Cl** and $K_{SV} = 2580 \pm 70$ bar^{-1} for **Pt–I** are identical within the experimental error limits. As expected from the longer triplet state lifetime, **Pt–NO$_2$** has an even larger K_{SV} of 2810 ± 110 bar^{-1}. Quenching constants evaluated by the ratios of lifetimes are somewhat smaller but still reach values of close to 2000 to 2200 bar^{-1}. All complexes show high sensitivities for small partial oxygen pressures. Above $p(O_2) = 0.1$ bar the plots start to deviate from linearity which relates to the low intensity of the residual signal. Our results render complexes **Pt–Cl**, **Pt–I** and **Pt–NO$_2$** particularly efficient oxygen sensors when compared to other
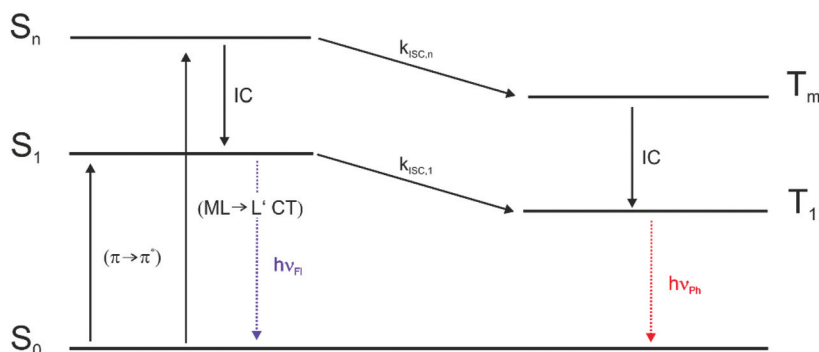
Scheme 1 Jablonski diagram for the relevant optical processes in the complexes *trans*-Pt(BODIPY)X(PEt$_3$)$_2$.
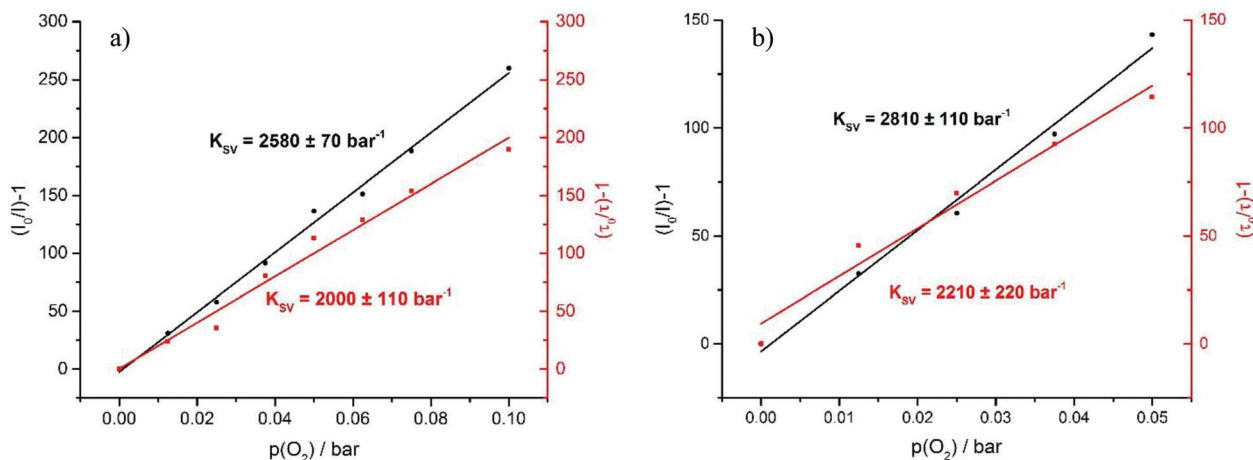
**Fig. 10** Stern–Volmer plot (a) of **Pt–I** and (b) of **Pt–NO$_2$**.

successful platinum-based systems.[49–54] We note here that a lower lifetime of the phosphorescence emission and hence lesser sensitivity towards O$_2$ quenching as it was observed for **Pt–Br** allows for O$_2$ detection in solution up to atmospheric concentration levels of the surrounding gas phase.

The feasibility of using these complexes as sensitizers for ^{1}O$_2$ generation from ^{3}O$_2$ by triplet–triplet annihilation in productive chemical reactions[55,56] such as the oxidation of 1,5-dihydroxynaphthalene (DHN) was investigated using the complexes **Pt–Cl** and **Pt–I** as catalysts. The catalytic cycle of the photocatalytic system consisting of the sensitizer, aereal O$_2$ and DHN is shown in Scheme 2. On the basis of this mechanism, the rate-law of DHN consumption can be written as $\nu_i = k_r$[O$_2$][DHN]. At the initial stage of the reaction oxygen concentration can be treated as constant. The previous equation can therefore be simplified to $\nu_i = k_{obs}\cdot$[DHN] using a pseudo first-order rate constant k_{obs}. Rewriting this formula as $\ln(C_t/C_0) = -k_{obs}\cdot t$, where C_t denotes the concentration of DHN at a certain reaction time t while C_0 is the initial concentration of DHN, allows for determining k_{obs} from the slope of a plot of $\ln(C_t/C_0)$ vs. reaction time t. The associated values of ν_i and the number of photons absorbed by the sensitizer provide the ^{1}O$_2$ generation quantum yield (Φ_Δ) by using the relative method

with methylene blue (MB) as a reference sensitizer.[57] Details of these experiments are provided in the Experimental section. Fig. 11a depicts the changes of the absorption spectra of the reaction mixture with irradiation time t using **Pt–Cl** as a sensitizer, while Fig. 11b compares plots of $\ln(C_t/C_0)$ as a function of t for **Pt–Cl**, **Pt–I** and the MB standard. The rate constants k_{obs}, the rates ν_i of DHN consumption, and quantum yields for the generation of ^{1}O$_2$ (Φ_Δ) in the photooxidation of DHN are summarized in Table 5. Both platinum complexes obey a linear relation between $\ln(C_t/C_0)$ and the irradiation time t from which ν_i was determined. This precludes side reactions and proves that the sensitizers are stable under these conditions. Control experiments in the absence of light showed that none of the sensitizers promotes oxidation of DHN to Juglone under dark conditions (see Fig. S38 and S39 in the ESI†). Both complexes show a significantly higher rate ν_i of DHN consumption than MB. Most remarkably, **Pt–I** and **Pt–Cl** have exceptionally high quantum efficiencies Φ_Δ of 0.95 (**Pt–I**) or even near unity (**Pt–Cl**) and clearly outperform the MB standard (Φ_Δ of 0.57).[58–60] Contributing factors are the high ISC efficiencies and the long lifetimes of the triplet state (τ_{Ph} = 277 μs for **Pt–Cl**, τ_{Ph} = 297 μs for **Pt–I**).

Summary and conclusions

We report on the synthesis and the spectroscopic and photophysical properties of five new complexes *trans*-Pt(BODIPY)X (PEt$_3$)$_2$ (**Pt–X**, X$^-$ = Cl$^-$, I$^-$, NO$_2^-$, NCS$^-$, CH$_3^-$). All contain a σ-bonded BODIPY ligand that binds to the platinum ion via its *meso* position. With the exception of **Pt–CH$_3$**, all complexes show dual fluorescence and phosphorescence emissions from the attached BODIPY dye at wavelengths that are largely invariant to the nature of the ligand X$^-$. Phosphorescence quantum yields and Pt–C(BODIPY) bond lengths increase in the order **Pt–NO$_2$** < **Pt–NCS** < **Pt–Cl** < **Pt–I** in parallel with the σ-*trans*-influence of the ligand X$^-$.
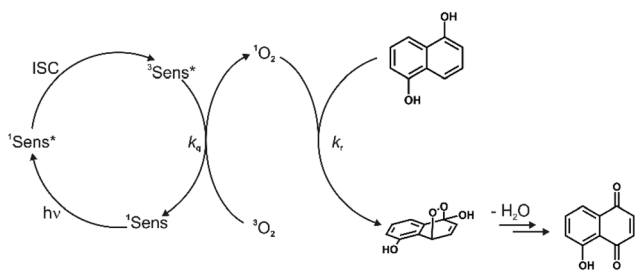
Scheme 2 Mechanism for the photooxidation of 1,5-dihydroxynaphthalene (DHN) by ^{1}O$_2$ catalyzed by a sensitizer, producing Juglone after the elimination of a water molecule.
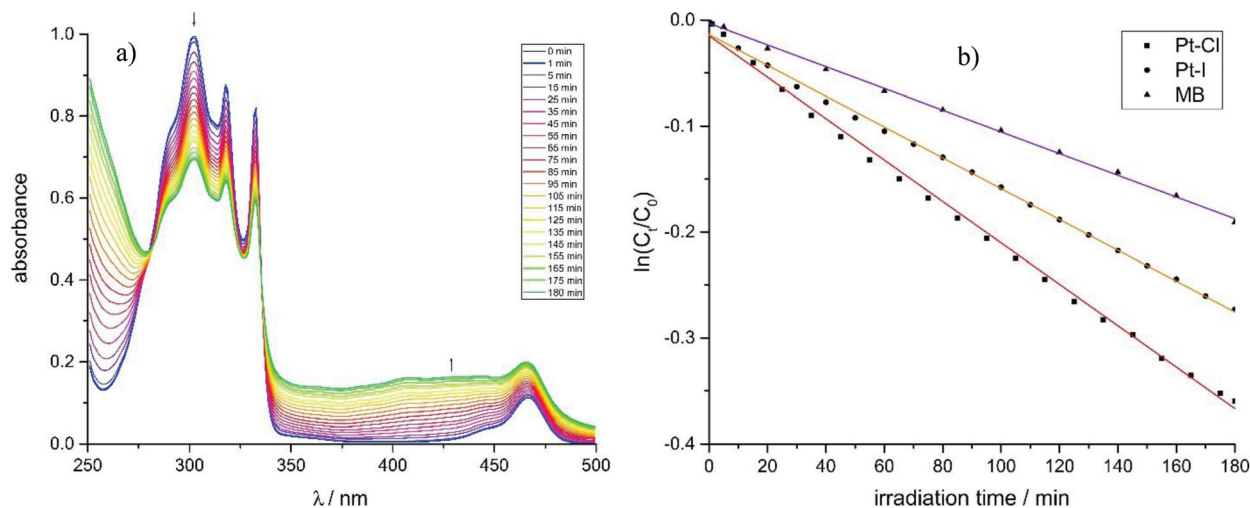
Fig. 11 (a) Spectral change in the UV-Vis region for the photooxidation of DHN using **Pt–Cl** as the sensitizer. (b) Plots of $\ln(C_t/C_0)$ vs. irradiation time for the photooxidation using complexes **Pt–Cl**, **Pt–I** and MB.

Table 5 Parameters of the pseudo first-order kinetics, $^1O_2$ generation quantum yields of the photooxidation of DHN using the complexes **Pt–Cl**, **Pt–I** (λ_{exc} = 460 nm) and MB (λ_{exc} = 655 nm) as sensitizers, and turnover frequency, as well as Stern–Volmer constants K_{SV} for the phosphorescence quenching of **Pt–Cl** and **Pt–I** by $^3O_2$

	k_{obs}[a] [min^{-1}]	ν_i[b] [×10^{-6} M min^{-1}]	I[c]	Φ_Δ[d]	Yield[e] [%]	TOF[f] [s^{-1}]	K_{SV}[g] [bar^{-1}]
Pt–Cl	0.00195	0.236	1.033	1.00	35	0.0019	2380 ± 170
Pt–I	0.00145	0.176	0.810	0.95	25	0.0014	2580 ± 70
MB	0.00102	0.130	1.000	0.57	14	0.0008	

[a] Pseudo first-order rate constant for DHN consumption. [b] Rate of DHN consumption. [c] Relative value of the number of photons absorbed by the sensitizer (I = 1 for the standard sensitizer MB). [d] Corrected $^1O_2$ generation quantum yield using the value of MB (Φ_Δ = 0.57)[58–60] as a reference. [e] Yield of Juglone after a reaction time of 180 min. [f] Turnover frequency. [g] In CH$_2$Cl$_2$ solution.

Most importantly, the ratio of phosphorescence to fluorescence intensities of each complex depends on the excitation wavelength. This is a direct consequence of the different natures of the initially populated excited states (BODIPY-based $\pi \rightarrow \pi^*$ or a higher excited state with appreciable Pt(PEt$_3$)$_2$ → BODIPY π^* ML → L′ charge-transfer character), which results in different rate constants k_{ISC}. Thus, the higher-energy MLCT absorption offers a more direct pathway for Pt-triggered ISC than just the heavy atom effect. Our present results provide experimental manifestation of the concept of excitation energy-dependent emission properties as recently discussed and observed by Chou and his coworkers.[33,45–47]

Additional studies into phosphorescence quenching by $^3O_2$ have yielded exceptionally large Stern–Volmer quenching constants of *ca.* 2000 bar^{-1} and demonstrated that these complexes are excellent one-component sensors for triplet molecules. Moreover, they constitute highly efficient sensitizers for photocatalytic reactions involving $^1O_2$ as the reactant, combining exceptionally high quantum efficiencies near unity for $^1O_2$ generation with good photostabilities. These treats will be further explored in our future work.

Experimental section

Materials and general methods

DHN was bought form Acros Organics and purified by sublimation (p = 4 × 10^{-3} mbar, 160° C oil bath). *cis*-Pt(BODIPY)Br(PEt$_3$)$_2$ was prepared as described elsewhere.[20] All manipulations where conducted under air except for reactions involving MeMgI, MgMe$_2$ and MeLi, which were performed under N$_2$ atmosphere by standard Schlenk techniques. Solvents for the reactions under inert gas atmosphere were distilled over adequate drying agents and stored under N$_2$ atmosphere. All other solvents were used as received from the suppliers.

NMR experiments were carried out on a Bruker Avance III DRX 400 or a Bruker Avance DRX 600 spectrometer. ^{1}H and ^{13}C NMR spectra were referenced to the solvent signal, while ^{31}P and ^{195}Pt NMR spectra were referenced using the Absolute Reference tool in the MestReNova software. NMR data are given as follows: chemical shift (δ in ppm), multiplicity (br, broad; d, doublet; dd, doublet of doublets; m, multiplet; s, singlet; t, triplet), integration, coupling constant (Hz). Unequivocal signal assignments were achieved by 2D NMR experiments. The numbering of the nuclei follows that of the crystal structures in

Fig. 3. Combustion analysis was conducted with an Elementar vario MICRO cube CHN-analyzer from Heraeus.

X-ray diffraction analysis of single crystals was performed at 100 K on a STOE IPDS-II diffractometer equipped with a graphite-monochromated radiation source (λ = 0.71073 Å) and an image plate detection system. A crystal mounted on a fine glass fiber with silicon grease was employed. If not indicated otherwise, the selection, integration, and averaging procedure of the measured reflex intensities, the determination of the unit cell dimensions and a least-squares fit of the 2θ values as well as data reduction, LP-correction, and space group determination were performed using the X-Area software package delivered with the diffractometer. A semiempirical absorption correction was performed.[61] All structures were solved by the heavy-atom methods (SHELXS-97, SHELXS-2013, or SHELXS-2014).[62,63] Structure solutions were completed with difference Fourier syntheses and full-matrix last-squares refinements using SHELXL-97, SHELXS-2013, or SHELXS-2014,[63] minimizing $\omega(F_o^2 - F_c^2)^2$. The weighted R factor (wR^2) and the goodness of the fit GOF are based on F^2. All non-hydrogen atoms were refined with anisotropic displacement parameters, while hydrogen atoms were treated in a riding model. Molecular structures in this work are plotted with ORTEP 32[64,65] or Mercury.[66] CIF files of **Pt–Cl**, **Pt–I**, **Pt–NCS**, **Pt–NO₂**, and **Pt–CH₃** have been deposited at the Cambridge Structure Data Base as CCDC 1474955 (**Pt–Cl**), 1474956 (**Pt–NCS**), 1474957 (**Pt–I**), 1474958 (**Pt–NO₂**), and 1474959 (**Pt–CH₃**).

UV-Vis absorption spectra were recorded on a TIDAS fiber-optic diode array spectrometer MCS from j&m in HELLMA quartz cuvettes with 1 cm optical path length at room temperature.

Computational details

The ground sate electronic structures were calculated by density functional theory (DFT) methods using the Gaussian 09[67] program packages. Quantum chemical studies were performed without any symmetry constraints. Open shell systems were calculated by the unrestricted Kohn-Sham approach (UKS).[68] Geometry optimization followed by vibrational analysis was made either in vacuum or in solvent media. The quasirelativistic Wood-Boring small-core pseudopotentials (MWB)[69,70] and the corresponding optimized set of basis functions[71] for Pt and the 6-31G(d) polarized double-ζ basis set[72] for the remaining atoms were employed together with the Perdew, Burke and Ernzerhof exchange and correlation functional (PBE1PBE).[73–75] Solvent effects were accounted for by the Polarizable Conductor Continuum Model (PCM)[76–78] with standard parameters for dichloromethane. Absorption spectra and orbital energies were calculated using time-dependent DFT (TD-DFT)[79] with the same functional/basis set combination as mentioned above. For easier comparison with the experiment, the obtained absorption and emission energies were converted into wavelengths and broadened by a Gaussian distribution (full width at half-maximum = 3000 cm⁻¹) using

the programm GaussSum.[80] Molecular orbitals were visualized with the GaussView programm[81] or with Avogadro.[82]

Luminescence spectroscopy and quenching experiments

All luminescence spectra and excited state lifetimes were recorded for *ca.* 10⁻⁶ M solutions in CH₂Cl₂ or toluene with a PicoQuant FluoTime 300 spectrometer at room temperature, if not stated otherwise. Luminescence experiments under inert gas atmosphere and defined O₂ concentrations were conducted in a quartz cuvette modified with an angle valve from Normag. Defined O₂ concentrations were adjusted by completely degassing the sample and subsequent injection of adequate volumes of air and nitrogen by syringe. Quantum yields were measured using a Hamamatsu Absolute PL Quantum Yield Measurement System C9920-02 equipped with an integrating sphere.

¹O₂ generation from Pt–X sensitizers

For the photoreactions involving ¹O₂ generation, a CH₂Cl₂/MeOH (9/1) solution containing DHN (1.2 × 10⁻⁴ M) and a sensitizer (1.7 mol% with respect to DHN) was irradiated in a quartz cell of 1 cm path length using the Xenon lamp of a PicoQuant FluoTime 300 spectrometer (λ_{ex}(**Pt–Cl, Pt–I**) = 460 ± 5 nm, I_f(460 ± 5 nm) = 1.3 mW; λ_{ex}(MB) = 655 ± 5 nm, I_f(655 ± 5 nm) = 580 μW). UV-Vis absorption spectra were recorded at intervals of 5–20 min on a Varian Cary 50 spectrometer. The consumption of DHN was monitored by the decrease of the absorption at 301 nm (ε = 7664 M⁻¹ cm⁻¹),[57] while Juglone production was monitored by an increase of the absorption at 427 nm (ε = 3811 M⁻¹ cm⁻¹).[57] The yield of Juglone was calculated from the concentration of Juglone and the initial concentration of DHN. The singlet oxygen quantum yield (Φ_Δ) was determined using eqn (1),[57,83]

$$\Phi_\Delta = \Phi_{\Delta,std}(\nu_i \cdot I_{std}/\nu_{i,std} \cdot I) \tag{1}$$

where $\Phi_{\Delta,std}$ is the singlet oxygen quantum yield of the standard sensitizer MB (Φ_Δ = 0.57),[58–60] ν_i is the rate of DHN consumption and I and I_{std} are the number of photons absorbed by the sensitizer and the standard, respectively. I was estimated from eqn (2) using the λ interval 455 to 465 nm for **Pt–Cl** and **Pt–I**, and 650 to 660 nm for MB,

$$I = \int I_f(\lambda) \, (1 - 10^{-\varepsilon(\lambda)C_s^l}) d\lambda \tag{2}$$

where $I_f(\lambda)$ is the wavelength dependence of the intensity of the incident light evaluated with a photometer (for values *vide supra*), $\varepsilon(\lambda)$ is the extinction coefficient of the respective sensitizer recorded in CH₂Cl₂/MeOH (9/1), C_s is the concentration of the sensitizer, and l is the length of the optical cell.

trans-Chloro-(4,4-difluoro-4-bora-3a,4a-diaza-*s*-indacen-8-yl)-bis(triethylphosphine)-platinum(ɪɪ) (Pt–Cl)

40 mg (57 μmol, 1 eq.) of *cis*-Pt(BODIPY)Br(PEt₃)₂ and 19.5 mg (76 μmol, 1.4 eq.) of AgOTf were dissolved in 0.8 ml of CD₂Cl₂. The solution was heated to reflux for 5 min which led to the

formation of *trans*-Pt(BODIPY)(OTf)(PEt$_3$)$_2$. The heterogeneous mixture was filtered and the filtrate was added to a solution of 66.6 mg (114 μmol, 2 eq.) of NaCl in 2.6 ml of MeOH. The orange suspension was stirred for 45 min. The solvents were then removed *in vacuo* and the solid was extracted with CH$_2$Cl$_2$. The product was purified by column chromatography (silica, CH$_2$Cl$_2$, R_f = 0.72). After washing with *n*-pentane (2 × 0.6 ml) the analytically pure product was obtained. Yield: 32%. Single crystals were obtained by slow evaporation of a CH$_2$Cl$_2$ solution. ^{1}H NMR (400 MHz, CD$_2$Cl$_2$): δ 7.65 (br s, 2H, H5, H9), 7.46 (d, 2H, $^3J_{HH}$ = 3.68 Hz, H3, H7), 6.46 (dd, 2H, $^3J_{HH}$ = 3.68 Hz, $^3J_{HH}$ = 2.04 Hz, H4, H8), 1.74 (m, 12H, P–C*H*$_2$–), 1.06 (dt, 18H, $^3J_{HH}$ = 7.66 Hz, $^3J_{PH}$ = 15.58 Hz, P–CH$_2$–C*H*$_3$). ^{31}P NMR (161.9 MHz, CD$_2$Cl$_2$): δ 11.70 (s, with satellites J_{PtP} = 2502 Hz). ^{13}C NMR (150.9 MHz, CD$_2$Cl$_2$): δ 178.5 (t, $^2J_{PC}$ = 7.8 Hz, with satellites J_{PtC} = 492 Hz, C1), 143.5 (s, with satellites $^2J_{PtC}$ = 22.4 Hz, C2, C6), 137.1 (s, C5, C9), 133.8 (s, with satellites $^3J_{PtC}$ = 25.2 Hz, C3, C7), 116.6 (s, C4, C8), 14.28 (t, J_{PC} = 33.0 Hz, with satellites $^2J_{PtC}$ = 17.0 Hz, P–C*H*$_2$–), 8.2 (t, $^2J_{PC}$ = 10.0 Hz, P–CH$_2$–C*H*$_3$). ^{195}Pt NMR (86.0 MHz, CD$_2$Cl$_2$): δ −4134 (t, J_{PtP} = 2502 Hz). C, H, N analysis calculated for C$_{21}$H$_{36}$ClBF$_2$N$_2$P$_2$Pt·0.3 C$_5$H$_{12}$: C, 39.77; H, 5.87; N, 4.12. Found: C, 39.44; H, 6.09; N, 4.06.

trans-Iodo-(4,4-difluoro-4-bora-3a,4a-diaza-*s*-indacen-8-yl)-bis(triethylphosphine)-platinum(II) (Pt–I)

trans-Pt(BODIPY)(OTf)(PEt$_3$)$_2$ prepared as described above was dissolved in 5 ml of dry THF under N$_2$ atmosphere. To this solution 0.08 ml of a freshly prepared 1 M MeMgI solution (1.4 eq.) in diethyl ether were added. The solution was stirred for 20 min, the precipitate was filtered off and the solution was evaporated to dryness.

The crude product was purified by column chromatography (silica deprotonated with 5% NEt$_3$, CH$_2$Cl$_2$: PE = 5 : 1, R_f = 0.46). After washing twice with 0.3 ml of *n*-pentane the yellow product was obtained in 58% yield. Single crystals suitable for X-ray diffraction analysis were obtained by slow evaporation of a C$_6$D$_6$ solution. ^{1}H NMR (400 MHz, C$_6$D$_6$): δ 7.81 (br s, 2H, H5, H9), 7.43 (d, 2H, $^3J_{HH}$ = 3.51 Hz, H3, H7), 6.19 (dd, 2H, $^3J_{HH}$ = 3.51 Hz, $^3J_{HH}$ = 1.89 Hz, H4, H8), 1.68 (m, 12H, P–C*H*$_2$–), 0.72 (dt, 18H, $^3J_{HH}$ = 7.68 Hz, $^3J_{PH}$ = 15.89 Hz, P–CH$_2$–C*H*$_3$). ^{31}P NMR (161.9 MHz, C$_6$D$_6$): δ 4.02 (s with satellites, J_{PtP} = 2450 Hz). ^{13}C NMR (100.6 MHz, C$_6$D$_6$): δ 181.1 (s, C1), 143.3 (s, C2, C6), 138.5 (s, C5, C9), 133.3 (s with satellites, $^3J_{PtC}$ = 25.0 Hz, C3, C7), 116.7 (s, C4, C8), 16.2 (t, J_{PC} = 34.2 Hz, with satellites $^2J_{PtC}$ = 17.6 Hz, P–C*H*$_2$–), 8.36 (t, $^2J_{PC}$ = 11.5 Hz, P–CH$_2$–C*H*$_3$). ^{195}Pt NMR (86.0 MHz, C$_6$D$_6$): δ −4503.4 (t, J_{PtP} = 2450 Hz). C, H, N analysis calculated for C$_{21}$H$_{36}$BF$_2$IN$_3$P$_2$Pt: C, 33.66; H, 4.84; N, 3.74. Found: C, 33.85; H, 5.06; N, 3.86.

trans-κ*N*-(4,4-difluoro-4-bora-3a,4a-diaza-*s*-indacen-8-yl)-(thiocyanato)-bis(triethylphosphine)-platinum(II) (Pt–NCS)

A solution of 30 mg (57 μmol, 1 eq.) of *cis*-Pt(BODIPY)Br(PEt$_3$)$_2$ and 19.5 mg (76 μmol, 1.4 eq.) of AgOTf in 0.8 ml of CH$_2$Cl$_2$ was refluxed for 5 min. The solution was filtered and 2.6 ml of a methanolic solution of NaSCN (9.2 mg, 114 μmol, 2 eq.) was

added. After stirring the reaction mixture for 1.5 h all volatiles were removed and the crude product was extracted with CH$_2$Cl$_2$. The product was further purified by column chromatography (silica deprotonated with 5% NEt$_3$, PE : EE = 3 : 1, R_f = 0.32). The product was washed with small amounts of *n*-pentane. Yield: 36%. Single crystals for X-ray diffraction analysis were obtained by slow evaporation of a CH$_2$Cl$_2$ solution. ^{1}H NMR (400 MHz, C$_6$D$_6$): δ 7.80 (br s, 2H, H5, H9), 7.28 (d, 2H, $^3J_{HH}$ = 3.67 Hz, H3, H7), 6.18 (dd, 2H, $^3J_{HH}$ = 3.67 Hz, $^3J_{HH}$ = 2.00 Hz, H4, H8), 1.27 (m, 12H, P–C*H*$_2$–), 0.68 (m, 18H, P–CH$_2$–C*H*$_3$). ^{31}P NMR (161.9 MHz, C$_6$D$_6$): δ 12.50 ppm (s, with satellites J_{PtP} = 2450 Hz). ^{13}C NMR (150.9 MHz, C$_6$D$_6$): δ 174.3 (s, C1), 143.4 (s, C2, C6), 138.3 (s, C5, C9), 132.5 (s, with satellites $^3J_{PtC}$ = 22.5 Hz, C3, C7), 116.7 (s, C4, C8), 14.6 (t, J_{PC} = 17.0 Hz, P–C*H*$_2$–), 7.6 (br s, P–CH$_2$–C*H*$_3$), signal for C10 not detected. ^{195}Pt NMR (129.0 MHz, C$_6$D$_6$): δ −4181.5 (t, J_{PtP} = 2450 Hz). C, H, N analysis calculated for C$_{22}$H$_{36}$BF$_2$N$_3$P$_2$PtS: C, 38.83; H, 5.33; N, 6.18. Found: C, 38.81; H, 5.59; N, 6.20.

trans-(4,4-Difluoro-4-bora-3a,4a-diaza-*s*-indacen-8-yl)-(nitrito)-bis(triethylphosphine)-platinum(II) (Pt–NO$_2$)

To *trans*-Pt(BODIPY)(OTf)(PEt$_3$)$_2$ prepared as described above from 40 mg (57 μmol, 1 eq.) of *cis*-Pt(BODIPY)Br(PEt$_3$)$_2$ in CH$_2$Cl$_2$, a solution of 7.9 mg (114 μmol, 2 eq.) of NaNO$_2$ in 2.6 ml of MeOH was added. The orange solution was stirred for 1.5 h at r.t., the solvents were removed and the crude solid was extracted with CH$_2$Cl$_2$. The product was purified by column chromatography (silica deprotonated with 5% NEt$_3$, PE : EE = 1 : 1, R_f = 0.41). After removing the solvent at low temperature the yellow product was washed two times with *n*-pentane and dried *in vacuo*. Yield: 26%. Single crystals for X-ray diffraction analysis were obtained by slow evaporation of a CH$_2$Cl$_2$ solution. ^{1}H NMR (400 MHz, C$_6$D$_6$): δ 7.81 (br s, 2H, H5, H9), 7.58 (d, 2H, $^3J_{HH}$ = 3.65 Hz, H3, H7), 6.22 (dd, 2H, $^3J_{HH}$ = 3.65 Hz, $^3J_{HH}$ = 1.89 Hz, H4, H8), 1.29 (m, 12H, P–C*H*$_2$–), 0.73 (m, 18H, P–CH$_2$–C*H*$_3$). ^{31}P NMR (161.9 MHz, C$_6$D$_6$): δ 9.69 (s, with satellites J_{PtP} = 2600 Hz). ^{13}C NMR (150.9 MHz, C$_6$D$_6$): δ 174.9 (t, $^2J_{PC}$ = 8.8 Hz, with satellites J_{PtC} = 409 Hz, C1), 143.5 (s, with satellites $^3J_{PtC}$ = 15.8 Hz, C2, C6), 138.6 (s, C5, C9), 133.2 (s, with satellites $^3J_{PtC}$ = 22.0 Hz, C3, C7), 116.7 (s, C4, C8), 14.7 (t, J_{PC} = 32.5 Hz, with satellites $^2J_{PtC}$ = 17.0 Hz, P–C*H*$_2$–), 7.6 (br s, P–CH$_2$–C*H*$_3$). ^{195}Pt NMR (129.0 MHz, C$_6$D$_6$): δ −4081.6 (t, J_{PtP} = 2600 Hz). C, H, N analysis calculated for C$_{21}$H$_{36}$BF$_2$N$_3$O$_2$P$_2$Pt: C, 37.74; H, 5.43; N, 6.29. Found: C, 37.78; H, 5.73; N, 6.40.

trans-(4,4-Difluoro-4-bora-3a,4a-diaza-*s*-indacen-8-yl)-(methyl)-bis(triethylphosphine)-platinum(II) (Pt–CH$_3$)

A CH$_2$Cl$_2$ solution containing 40 mg (57 μmol, 1 eq.) of *cis*-Pt(BODIPY)Br(PEt$_3$)$_2$ and 19.5 mg (76 μmol, 1.4 eq.) of AgOTf was refluxed for 5 min, then filtered and evaporated to dryness. The crude solid was placed under nitrogen atmosphere, 10 ml of diethyl ether were added and the solution was cooled to −78° C. To this bright orange solution 0.5 ml of a 0.18 M solution of methyl lithium in diethyl ether was added dropwise. The reaction mixture turned green while it was

allowed to warm to room temperature over 4 h. The mixture was filtered, the solvent was removed and the crude solid was purified by column chromatography (silica deprotonated with 5% NEt_3, petroleum ether : ethyl acetate = 8 : 3, R_f = 0.73). The product was washed two times with *n*-pentane and dried *in vacuo*. Yield: 49%. Single crystals were obtained by slow diffusion of *n*-pentane in a saturated C_6D_6 solution. ^1H NMR (600 MHz, C_6D_6): δ 7.92 (br s, 2H, H5, H9), 7.47 (d, 2H, $^3J_{HH}$ = 3.48 Hz, C3, C7), 6.31 (dd, 2H, $^3J_{HH}$ = 3.48 Hz, $^3J_{HH}$ = 2.05 Hz, H4, H8), 1.35 (m, 12H, P–CH_2–), 0.70 (dt, 18H, $^3J_{HH}$ = 7.67 Hz, $^3J_{PH}$ = 15.68 Hz, P–CH$_2$–CH_3), −0.24 (t with satellites, 3H, $^3J_{PH}$ = 6.82 Hz, $^2J_{PtH}$ = 24.9 Hz, CH_3). ^{31}P NMR (161.9 MHz, C_6D_6): δ 9.18 (s, with satellites J_{PtP} = 2692 Hz). ^{13}C NMR (150.9 MHz, C_6D_6): δ 210.6 (t, $^2J_{PC}$ = 9.41 Hz, C1), 146.4 (s with satellites, $^2J_{PtC}$ = 22.0 Hz, C2, C6), 136.4 (s, C5, C9), 132.2 (s with satellites, $^3J_{PtC}$ = 37.0 Hz, C3, C7), 115.6 (s, C4, C8), 14.3 (t with satellites, J_{PC} = 17.0 Hz, $^2J_{PtC}$ = 67.1 Hz, P–CH_2–), 8.0 (s with satellites, $^3J_{PtC}$ = 25.5 Hz, P–CH$_2$–CH_3), −14.0 (t, $^2J_{PC}$ = 8.80 Hz, with satellites J_{PtC} = 412.7 Hz, C10). ^{195}Pt NMR (86.0 MHz, C_6D_6): δ −4396 (t, J_{PtP} = 2692 Hz). C, H, N analysis calculated for $C_{22}H_{39}BF_2N_2P_2Pt$: C, 41.46; H, 6.17; N, 4.39. Found: C, 41.34; H, 6.47; N, 4.51.

Notes

The authors declare no competing financial interest.

Acknowledgements

References

1 A. Treibs and F.-H. Kreuzer, *Liebigs Ann. Chem.*, 1968, **718**, 208–223.

2 A. Loudet and K. Burgess, *Chem. Rev.*, 2007, **107**, 4891–4932.

3 G. Ulrich, R. Ziessel and A. Harriman, *Angew. Chem., Int. Ed.*, 2008, **47**, 1184–1201.

4 N. Boens, B. Verbelen and W. Dehaen, *Eur. J. Org. Chem.*, 2015, 6577–6595.

5 F. Li, S. I. Yang, Y. Ciringh, J. Seth, C. H. Martin, D. L. Singh, D. Kim, R. R. Birge, D. F. Bocian, D. Holten and J. S. Lindsey, *J. Am. Chem. Soc.*, 1998, **120**, 10001–10017.

6 J. Chen, A. Burghart, A. Derecskei-Kovacs and K. Burgess, *J. Org. Chem.*, 2000, **65**, 2900–2906.

7 F. E. Alemdaroglu, S. C. Alexander, D. Ji, D. K. Prusty, M. Börsch and A. Herrmann, *Macromolecules*, 2009, **42**, 6529–6536.

8 M. T. Whited, P. I. Djurovich, S. T. Roberts, A. C. Durrell, C. W. Schlenker, S. E. Bradforth and M. E. Thompson, *J. Am. Chem. Soc.*, 2011, **133**, 88–96.

9 R. Ziessel, G. Ulrich, A. Haefele and A. Harriman, *J. Am. Chem. Soc.*, 2013, **135**, 11330–11344.

10 T. Lazarides, T. M. McCornick, K. C. Wilson, S. Lee, D. W. McCamant and R. Eisenberg, *J. Am. Chem. Soc.*, 2011, **133**, 350–364.

11 M. Cordaro, P. Mineo, F. Nastasi and G. Magazzu, *RSC Adv.*, 2014, **4**, 43931–43933.

12 N. Boens, V. Leen and W. Dehaen, *Chem. Soc. Rev.*, 2012, **41**, 1130–1172.

13 T. Yogo, Y. Urano, Y. Ishitsuka, F. Maniwa and T. Nagano, *J. Am. Chem. Soc.*, 2005, **127**, 12162–12163.

14 J. Zhao, K. Xu, W. Yang, Z. Wang and F. Zhong, *Chem. Soc. Rev.*, 2015, **44**, 8904–8939.

15 A. Gorman, J. Killoran, C. O'Shea, T. Kenna, W. M. Gallagher and D. F. O'Shea, *J. Am. Chem. Soc.*, 2004, **126**, 10619–10631.

16 X.-F. Zhang and X. Yang, *J. Phys. Chem. B*, 2013, **117**, 5533–5539.

17 W. Wu, J. Zhao, J. Sun, L. Huang and X. Yi, *J. Mater. Chem. C*, 2013, **1**, 705–716.

18 W. Wu, J. Zhao, H. Guo, J. Sun, S. Ji and Z. Wang, *Chem. – Eur. J.*, 2012, **18**, 1961–1968.

19 J. Sun, F. Zhong, X. Yi and J. Zhao, *Inorg. Chem.*, 2013, **52**, 6299–6310.

20 F. Geist, A. Jackel and R. F. Winter, *Inorg. Chem.*, 2015, **54**, 10946–10957.

21 P. Batat, M. Cantuel, G. Jonusauskas, L. Scarpantonio, A. Palma, D. F. O'Shea and N. D. McClenaghan, *J. Phys. Chem. A*, 2011, **115**, 14034–14039.

22 X.-D. Wang and O. S. Wolfbeis, *Chem. Soc. Rev.*, 2014, **43**, 3666–3761.

23 W. Wu, J. Sun, X. Cui and J. Zhao, *J. Mater. Chem. C*, 2013, **1**, 4577–4589.

24 S. G. Awuah and Y. You, *RSC Adv.*, 2012, **2**, 11169–11183.

25 A. Kamkaew, S. H. Lim, H. B. Lee, L. V. Kiew, L. Y. Chung and K. Burgess, *Chem. Soc. Rev.*, 2013, **42**, 77–88.

26 R. Bonnett, *Chem. Soc. Rev.*, 1995, **24**, 19–33.

27 T. J. Dougherty, C. J. Gomer, B. W. Henderson, G. Jori, D. Kessel, M. Korbelik, J. Moan and Q. Peng, *J. Natl. Cancer Inst.*, 1998, **90**, 889–905.

28 D. E. J. G. J. Dolmans, D. Fukumura and R. K. Jain, *Nat. Rev. Cancer*, 2003, **3**, 380–387.

29 P. Agostinis, K. Berg, K. A. Cengel, T. H. Foster, A. W. Girotti, S. O. Gollnick, S. M. Hahn, M. R. Hamblin, A. Juzeniene, D. Kessel, M. Korbelik, J. Moan, P. Mroz, D. Nowis, J. Piette, B. C. Wilson and J. Golab, *CA – Cancer J. Clin.*, 2011, **61**, 250–281.

30 W. H. Lam, E. S.-H. Lam and V. W.-W. Yam, *J. Am. Chem. Soc.*, 2013, **135**, 15135–15143.

31 J. A. G. Williams, *Top. Curr. Chem.*, 2007, **281**, 205–268.

32 V. W.-W. Yam and K. M.-C. Wong, *Chem. Commun.*, 2011, **47**, 11579–11592.

33 P.-T. Chou, Y. Chi, M.-W. Chung and C.-C. Lin, *Coord. Chem. Rev.*, 2011, **255**, 2653–2665.

34 F. Geist, A. Jackel and R. F. Winter, *Dalton Trans.*, 2015, **44**, 3974–3987.

35 T. G. Appleton, H. C. Clark and L. E. Manzer, *Coord. Chem. Rev.*, 1973, **10**, 335–422.

36 T. J. McCarthy, R. G. Nuzzo and G. M. Whitesides, *J. Am. Chem. Soc.*, 1981, **103**, 3396–3403.

37 S. Lentijo, J. A. Miguel and P. Espinet, *Inorg. Chem.*, 2010, **49**, 9169–9177.

38 P. Nilsson, F. Plamper and O. F. Wendt, *Organometallics*, 2003, **22**, 5235–5242.

39 R. Bardi and A. M. Piazzesi, *Inorg. Chim. Acta*, 1981, **47**, 249–254.

40 C. Albrecht, C. Wagner, K. Merzweiler, T. Lis and D. Steinborn, *Appl. Organomet. Chem.*, 2005, **19**, 1155–1163.

41 S. J. Anderson and R. J. Goodfellow, *J. Chem. Soc., Dalton Trans.*, 1977, 1683–1686.

42 J. L. Burmeister and F. Basolo, *Inorg. Chem.*, 1964, **3**, 1587–1593.

43 E. Hartmann and R. M. Gschwind, *Angew. Chem., Int. Ed.*, 2013, **52**, 2350–2354.

44 C. Hansch, A. Leo and R. W. Taft, *Chem. Rev.*, 1991, **91**, 165–195.

45 C.-W. Hsu, C.-C. Lin, M.-W. Chung, Y. Chi, G.-H. Lee, P.-T. Chou, C.-H. Chang and P.-Y. Chen, *J. Am. Chem. Soc.*, 2011, **133**, 12085–12099.

46 C.-C. Hsu, C.-C. Lin, P.-T. Chou, C.-H. Lai, C.-W. Hsu, C.-H. Lin and Y. Chi, *J. Am. Chem. Soc.*, 2012, **134**, 7715–7724.

47 Y.-C. Chang, K.-C. Tang, H.-A. Pan, S.-H. Liu, I. O. Koshevoy, A. J. Karttunen, W.-Y. Hung, M.-H. Cheng and P.-T. Chou, *J. Phys. Chem. C*, 2013, **117**, 9623–9632.

48 E. Yu-Tzu Li, T.-Y. Jiang, Y. Chi and P.-T. Chou, *Phys. Chem. Chem. Phys.*, 2014, **16**, 26184–26192.

49 W. Wu, C. Cheng, W. Wu, H. Guo, S. Ji, P. Song, K. Han, J. Zhao, X. Zhang, Y. Wu and G. Du, *Eur. J. Inorg. Chem.*, 2010, **2010**, 4683–4696.

50 W. Wu, W. Wu, S. Ji, H. Guo, P. Song, K. Han, L. Chi, J. Shao and J. Zhao, *J. Mater. Chem.*, 2010, **20**, 9775–9786.

51 Y. Liu, H. Guo and J. Zhao, *Chem. Commun.*, 2011, **47**, 11471–11473.

52 W. Wu, W. Wu, S. Ji, H. Guo and J. Zhao, *Dalton Trans.*, 2011, **40**, 5953–5963.

53 H. Sun, H. Guo, W. Wu, X. Liu and J. Zhao, *Dalton Trans.*, 2011, **40**, 7834–7841.

54 H. Xiang, L. Zhou, Y. Feng, J. Cheng, D. Wu and X. Zhou, *Inorg. Chem.*, 2012, **51**, 5208–5212.

55 H. Wasserman and R. W. Murray, *Singlet Oxygen*, Academic Press, New York, 1979.

56 H. H. Wasserman and J. L. Ives, *Tetrahedron*, 1981, **37**, 1825–1852.

57 S.-Y. Takizawa, R. Aboshi and S. Murata, *Photochem. Photobiol. Sci.*, 2011, **10**, 895–903.

58 Y. Usui, *Chem. Lett.*, 1973, **2**, 743–744.

59 F. Wilkinson, W. P. Helman and A. B. Ross, *J. Phys. Chem. Ref. Data*, 1993, **22**, 113–262.

60 J. N. Chaon, G. R. Jamieson and R. S. Sinclair, *Chem. Phys. Lipids*, 1987, **43**, 81–99.

61 W. Herrendorf and W. Bärnighausen, *X-Area, Version 1.06*, Stoe, Darmstadt, Karslruhe, Gießen, 1999.

62 G. M. Sheldrick, *SHELXL-97, Program for Crystal Structure Solution and Refinement*, Universität Göttingen, 1997.

63 G. M. Sheldrick, *Acta Crystallogr., Sect. A: Fundam. Crystallogr.*, 2008, **64**, 112–122.

64 L. J. Farrugia, *J. Appl. Crystallogr.*, 1997, **30**, 565.

65 L. J. Farrugia, *J. Appl. Crystallogr.*, 2012, **45**, 849–854.

66 P. R. Edgington, P. McCabe, C. F. Macrae, E. Pidcock, G. P. Shields, R. Taylor, M. Towler and J. Van De Streek, *J. Appl. Crystallogr.*, 2006, **39**, 453–457.

67 M. J. Frisch, G. Trucks, H. B. Schlegel, G. E. Scuseria, M. A. Robb, J. R. Cheeseman, G. Scalmani, V. Barone, B. Mennucci, G. A. Petersson, H. Nakatsuji, M. Caricato, X. Li, H. P. Hratchian, A. F. Izmaylov, J. Blonio, G. Zheng, J. L. Sonnenberg, M. Hada, M. Ehara, K. Toyota, R. Fukuda, J. Hasegawa, M. Ishida, T. Nakajima, Y. Honda, O. Kitao, H. Nakai, T. Vreven, J. A. M. Jr., J. E. Peralta, F. Ogliaro, M. Bearpark, J. J. Heyd, E. Brothers, K. N. Kudin, V. N. Staroverov, R. Kobayashi, J. Normand, K. Raghavachari, A. Rendell, J. C. Burant, S. S. Iyengar, J. Tomasi, M. Cossi, N. Rega, J. M. Millam, M. Klene, J. E. Knox, J. B. Cross, V. Bakken, C. Adamo, J. Jaramillo, R. Gomperts, R. E. Stratmann, O. Yazyev, A. J. Austin, R. Cammi, C. Pomelli, J. W. Ochterski, R. L. Martin, K. Morokuma, V. G. Zakrzewski, G. A. Voth, P. Salvador, J. J. Dannenberg, S. Dapprich, A. D. Daniels, Ö. Farkas, J. B. Foresman, J. V. Ortiz, J. Cioslowski and D. J. Fox, *Gaussian 09, Revision C.01*, Gaussian, Inc., Wallingford, CT, USA, 2009.

68 O. Gunnarsson and B. I. Lundqvist, *Phys. Rev. B: Solid State*, 1976, **13**, 4274.

69 W. Küchle, M. Dolg, H. Stoll and H. Preuss, *J. Chem. Phys.*, 1994, **100**, 7535–7532.

70 M. Dolg, H. Stoll and H. Preuss, *J. Chem. Phys.*, 1989, **90**, 1730–1734.

71 D. Andrae, U. Haeussermann, M. Dolg, H. Stoll and H. Preuss, *Theor. Chim. Acta*, 1990, **77**, 123.

72 P. H. Hariharan and J. A. Pople, *Theor. Chim. Acta*, 1973, **28**, 213–222.

73 J. P. Perdew, K. Burke and M. Enzerhof, *Phys. Rev. Lett.*, 1996, **77**, 3865–3868.

74 J. P. Perdew, K. Burke and M. Ernzerhof, *Phys. Rev. Lett.*, 1997, **78**, 1396–1396.

75 C. Adamo and V. Barone, *J. Chem. Phys.*, 1999, **110**, 6158–6170.

76 E. Cancés, B. Menucci and J. Tomasi, *J. Chem. Phys.*, 1997, **107**, 3032–3041.

77 B. Mennucci and J. Tomasi, *J. Chem. Phys.*, 1997, **106**, 5151–5158.

78 M. Cossi, N. Rega, G. Scalmani and V. Barone, *J. Comput. Chem.*, 2003, **24**, 669–681.

79 E. Runge and K. U. G. E, *Phys. Rev. Lett.*, 1984, **52**, 997–1000.

80 N. M. O'Boyle, A. L. Tenderholt and K. M. Langner, *J. Comput. Chem.*, 2008, **29**, 839–845.

81 T. Keith and J. Millam, *GaussView, Version 3*, Shawnee Mission, KS, USA, 2009.

82 M. D. Hanwell, D. E. Curtis, D. C. Lonie, T. Vandermeersch, E. Zurek and G. R. Hutchinson, *J. Cheminf.*, 2012, **4**, 17.

83 N. Adarsh, M. Shanmugasundaram, R. R. Avirah and D. Ramaiah, *Chem. – Eur. J.*, 2012, **18**, 12655–12662.